JOURNAL OF GUIDANCE, CONTROL, AND DYNAMICS
Vol. 33, No. 1, January–February 2010

Flight Control for Flexible, High-Aspect-Ratio Flying Wings

Brijesh Raghavan* and Mayuresh J. Patil†
Virginia Polytechnic Institute and State University, Blacksburg, Virginia 24061-0203.

DOI: 10.2514/1.45471

High-aspect-ratio flying wing configurations designed for high altitude, long endurance missions are characterized by high flexibility, which may lead to significant static aeroelastic deformation and coupling between aeroelasticity and flight dynamics. Using the concept of the mean axis, a 6-degree-of-freedom reduced-order model of the flight dynamics is constructed that minimizes the coupling between rigid-body modes and structural dynamics while accounting for the nonlinear static aeroelastic deformation of the flying wing. A multistep nonlinear dynamic inversion controller based on this reduced-order model is coupled with a nonlinear guidance law to design a flight controller for path following. The configuration of the flying wing used in the reduced-order model is updated at each time instant to account for static aeroelastic deformation. Simulation results presented in this paper show that the controller is able to successfully follow both straight line and curved ground paths while maintaining/moving to the desired altitude. The controller is also shown to be able to handle an abrupt change in the external loading, which is simulated by a step change in the payload mass.

Nomenclature

a	=	computed acceleration
$\mathcal{C}$	=	rotation matrix
$\mathbf{f}$	=	external force
$\mathbf{H}$	=	angular momentum
h	=	altitude
$\mathcal{I}$	=	moment of inertia
$\mathbb{I}$	=	3×3 identity matrix
K	=	gain value
L	=	reference length
M	=	mass
$\mathbf{m}$	=	external moment
$\mathbf{P}$	=	linear momentum
$\mathbf{r}$, $\mathbf{R}$	=	position vector
T	=	thrust value
$\mathbf{V}$	=	linear velocity
γ	=	flight path angle
ΔT	=	differential thrust
δ	=	control surface deflection
μ	=	mass per unit length
ξ	=	center of mass offset
χ	=	yaw angle of velocity vector in inertial frame
ψ, θ, ϕ	=	yaw, pitch and roll angles, respectively
$\mathbf{\Omega}$	=	angular velocity

Subscript

a	=	deflection for roll control
c	=	value commanded by dynamic inversion
cg	=	corresponding to the center-of-gravity
e	=	deflection for pitch control
g	=	component in the inertial XY plane
M	=	corresponding to mean reference frame
mi	=	inertial to mean axis transformation
∞	=	freestream condition

Superscripts

d	=	demanded rate
M	=	mean axis components of a vector (appears as a left-hand superscript)
n	=	nth node/element

Presented at the International Forum of Aeroelasticity and Structural Dynamics, Seattle, WA, 21–25 June 2009; received 15 May 2009; revision received 7 Aug. 2009; accepted for publication 7 Aug. 2009.

*Graduate Student, Department of Aerospace and Ocean Engineering; brijeshr@vt.edu. Student Member AIAA.

†Assistant Professor, Department of Aerospace and Ocean Engineering; mpatil@vt.edu. Senior Member AIAA.

I. Introduction

A. Motivation

HIGH altitude, long endurance (HALE) unmanned aerial vehicles (UAV)s are designed to loiter above 60,000 ft and fly missions ranging from a few days to a few years. This unique flight profile makes it possible to use these aircraft as platforms for scientific research, aerial photography, and telecommunication relay. The demand for these capabilities in both the civilian and the military sectors has been the motivation for the development of HALE UAVs over the past two decades.

The Environmental Research Aircraft and Sensor Technology (ERAST) program was conducted by NASA from 1994 to 2003 with the primary objective of developing HALE UAVs. As part of this program, AeroVironment, Inc., developed a series of solar-powered flying wing configurations, for which the aspect ratio increased progressively from 12 to 30.9, along with a corresponding increase in payload capability. The final airplane in this series, Helios, crashed during a flight test off the island of Kauai, Hawaii, on 26 June 2003 [1]. The airplane deformed into an "unexpected, persistent, high dihedral" configuration on encountering turbulence, which in turn led to unstable pitch oscillations and finally resulted in the crash. The mishap investigation report concluded that the decision to test fly the crashed configuration was a flawed one, but it had been made because available analysis tools were unable to predict that predict the sensitivity of the configuration to disturbances. The report further suggested the development of "more advanced, multidisciplinary (structures, aeroelastic, aerodynamics, atmospheric, materials, propulsion, controls, etc.) 'time-domain' analysis methods appropriate to highly flexible, 'morphing' vehicles"[1].

B. Literature Review

This subsection presents a brief review of previous work on the application of nonlinear dynamic inversion based flight controllers to flexible airplanes, and flight control of highly flexible HALE configurations.

Over a series of three papers, Gregory addressed the problem of applying a dynamic inversion to control a large flexible aircraft [2–4].

The modified dynamic inversion controller presented in the first paper was designed to follow control inputs while minimizing elastic deflections at the front end of the fuselage. The controller was designed on a longitudinal model with eight elastic modes and applied on a longitudinal model with 20 elastic modes. The dependence of longitudinal and elastic modal states on actuator rates and accelerations was also modeled. These effects may not be insignificant for an elastic airplane due to unsteady aerodynamic and mass coupling effects. It was found that the stability augmentation system and structural modal system had to be designed in an integrated fashion, as the stand-alone stability augmentation system used for comparison drove the fuselage structural modes unstable and drove one of the control surfaces to its rate limit [2]. The next paper in the series dealt with the modification introduced in the dynamic inversion control law to make it applicable to the flexible configuration [3]. It was shown that the time constant of a first-order filter, introduced in the dynamic inversion loop, changed the damping of a flexible mode in a stand alone second-order flexible model. This influence of the first-order filter on the damping of the flexible mode was also found in the complete elastic model of the airplane. It was also found that individual dynamics can be controlled by changing the corresponding filter time constant although leaving the other filter time constants unchanged. The final paper in the series presented stability results for the dynamic inversion controller as applied to the flexible aircraft problem [4]. Results were presented for a simplified model. Only one flexible mode was modeled along with longitudinal dynamics, and the control law was designed only for flight control. The analysis considered only the dynamic inversion part of the controller and the part specifying the desired dynamics was not analyzed.

Shearer and Cesnik studied the open-loop response of a wing-body HALE configuration in the time domain to control inputs in the longitudinal and lateral-directional planes [5]. A time marching algorithm was implemented on a full nonlinear model, a linearized model, and a reduced-order model. For the representative configuration considered in the paper, they found that a linearized model was necessary for analyzing maneuvers in the plane of symmetry, and the full nonlinear model was necessary for analyzing asymmetric maneuvers. This work was extended by the authors to control system design for a wing-body HALE configuration [6]. A flight controller was designed to be effective in the absence of divergence, flutter, or limit cycle oscillations (LCO)s. The controller used a two-loop process with a fast inner-loop control for the dynamics of the airplane and a slow outer-loop control using a proportional integral derivative (PID) design for controlling flight path angle, Euler roll angle, and the corresponding rates. Unsteady aerodynamic effects were neglected during the design of the controller. Longitudinal and lateral modes were decoupled, and it was assumed that longitudinal modes were not affected by elastic states. A linear quadratic regulator (LQR) controller was designed for lateral dynamics, and a nonlinear dynamic inversion controller was designed for longitudinal dynamics. For the design of the controller for lateral dynamics, full state feedback including elastic states was assumed. The nonlinear dynamic inversion controller for longitudinal dynamics was designed only over rigid-body states. A third-order low-pass Butterworth filter was used to eliminate high-frequency numerical error generated during simulations. Simulation results were presented for turning flight with altitude change in full fuel and empty fuel conditions.

C. Objectives

A low weight, high-aspect-ratio wing design exhibits high flexibility and may undergo significant deformation in flight. Moreover, the aeroelastic and flight dynamics frequencies may overlap resulting in coupling of the flight dynamics and aeroelastic modes. If either one or both these characteristics are exhibited by an airplane configuration, it becomes necessary to model the aeroelasticity and flight dynamics in an integrated manner. Such an integrated model was developed by Patil and Hodges in 2003 for a high aspect-ratio, flexible flying wing configuration [7] and will be used to carry out time-marching simulations in this paper.

Previous work by the authors had shown that a rigid-body model that accounted for static aeroelastic deformation could capture the predominant flight dynamic characteristics exhibited by the integrated aeroelastic and flight dynamic model of the HALE flying wing [8]. Therefore, even in the presence of coupling between aeroelasticity and flight dynamics, a reduced-order model can be used for flight control design if it captures the rigid-body modes and static aeroelastic deformation of the flying wing and minimizes the interaction between structural dynamics and the rigid-body modes. This is accomplished by writing the equations of motion in the mean axis system as shown in section III.B of this paper.

The objective of this paper is the design of a flight control system for path following for a flexible, high aspect-ratio flying wing. Multistep nonlinear dynamic inversion was previously applied by Snell et al. [9] and Bugajski and Enns [10] to a rigid-body flight dynamics model. Building on these results [8–10], the flight control system presented in this paper is designed by the application of multistep nonlinear dynamic inversion to a 6-degree-of-freedom reduced-order model written in the mean axis system. The configuration of the flying wing used in the reduced-order model is updated at each time step to account for static aeroelastic deformation. The controller is then coupled to a nonlinear guidance law developed by Park et al. [11] which showed superior performance compared with linear guidance laws for following curved ground paths.

The results section of this paper presents the control inputs and the closed-loop response for the flexible flying wing for path following for a straight-line ground path and for a curved ground path. The performance of the controller in the presence of an abrupt change in external loading is studied by simulating a step change in the payload mass.

The work presented in this paper is directly applicable to unswept, high aspect-ratio, highly flexible flying wings for which the structure can be accurately modeled using nonlinear beam theory, and for which the aerodynamics is captured by 2-D, unsteady, incompressible, potential flow models. The applicability of the flight dynamic analysis and the flight control design presented here will have to be reviewed for a flying wing which does not satisfy any of the assumptions mentioned earlier.

II. Integrated Model of Aeroelasticity and Flight Dynamics

The integrated aeroelastic model used for time-marching simulations in this paper was developed by Patil and Hodges [7]. Details of the modeling are given in the original reference and will not be repeated in this paper.

The flying wing configuration used in this paper has five engines evenly spaced along the wing span as shown in Fig. 1. The entire trailing edge is actuated and is split into two sections along the span. The two sections deflect in the same direction for pitch control and differentially for roll control. The total control surface deflection for each section is calculated by summing these two components. As the flying wing does not have a rudder or vertical tail, yaw control is obtained by linearly redistributing thrust across the different engines. The differential thrust ΔT is chosen such that it is zero at the center and changes by integral multiples across the wingspan.

III. Control System Design

A. Overview

The objective of the control system is to track a predefined trajectory on the ground while maintaining a specified flight speed

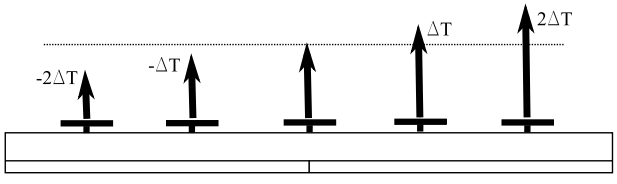

Fig. 1 Differential thrust for yaw control.

and altitude. This is accomplished by a combination of a nonlinear guidance algorithm [11] and a multiloop dynamic inversion controller [9,10] applied to the equations of motion of the flexible airplane written in the mean axis system. The use of the mean axis system to write the equations of motion eliminates the structural/inertial coupling between the rigid-body modes and the structural dynamics of the deformed airplane [12], resulting in a reduced-order system with only 6-degrees-of-freedom. The effect of static aeroelastic deformation on the flight dynamics is accounted for by calculating the aerodynamics based on the deformed shape and by recalculating the center of gravity and the total moment of inertia of the airplane at every time instant. Nonlinear dynamic inversion applied to this 6-degree-of-freedom reduced-order model of the statically deformed airplane cancels the inherent dynamics of the system and replaces it with prescribed dynamics.

B. Mean Axis Model

The concept of the mean axis was used by Milne to study the dynamics of a deformable airplane by assuming small deformation [12]. The mean axis system is defined as a system with respect to which the motion due to deformation has zero linear and angular momentum. If small deformation is assumed, the use of the mean axis system structurally and inertially decouples the equations for flight dynamics from the equations for structural dynamics. In the following sections, the equations for flight dynamics are derived in the mean axis for a generic discretized model without making a small-deformation assumption. Only the significant steps of the derivation are provided in this paper. A detailed derivation is given in Ref. [13].

1. *Equations of Motion*

Consider a set of rigid bodies each with its associated local reference frame B as shown in Fig. 2. For the nth rigid body, denote the mass by μ^n, the moment-of-inertia matrix about its center of gravity by $\mathcal{I}^n$, the velocity vector by $\mathbf{V}^n$, and the angular velocity vector by $\boldsymbol{\Omega}^n$. Represent the forces and moments acting on the nth rigid body by $\mathbf{f}^n$ and $\mathbf{m}^n$, respectively. Define a noninertial reference frame O for which the origin is at a distance $\mathbf{R}_O$ from the origin of the inertial reference frame I. Denote the position of the center of gravity of the nth body in the O frame by $\mathbf{r}^n$ and in the inertial frame by $\mathbf{R}^n$. These three vectors are now related as

$$\mathbf{R}^n = \mathbf{R}_O + \mathbf{r}^n$$

The total linear momentum of the set of bodies is now given by

$$\mathbf{P} = \sum \mu^n \frac{\mathrm{d}}{\mathrm{d}t}\bigg|_I \mathbf{R}^n = \sum \mu^n \mathbf{V}^n \tag{1}$$

which can also be written as

$$\begin{aligned}\mathbf{P} &= \sum \mu^n \tfrac{\mathrm{d}}{\mathrm{d}t}\Big|_I (\mathbf{R}_O + \mathbf{r}^n) = \sum \mu^n \tfrac{\mathrm{d}}{\mathrm{d}t}\Big|_I \mathbf{R}_O + \sum \mu^n \tfrac{\mathrm{d}}{\mathrm{d}t}\Big|_I \mathbf{r}^n \\ &= M_{\text{total}}\mathbf{V}_O + \sum \mu^n \frac{\mathrm{d}}{\mathrm{d}t}\bigg|_I \mathbf{r}^n \end{aligned} \tag{2}$$

where M_{total} is the total mass of the system, and $\mathbf{V}_O$ represents the velocity of the origin of the O frame. Representing the position of the center of gravity of the set of bodies in the O frame by ξ_O, the following relation can be obtained:

$$\sum \mu^n \frac{\mathrm{d}}{\mathrm{d}t}\bigg|_I \mathbf{r}^n = \frac{\mathrm{d}}{\mathrm{d}t}\bigg|_I \sum \mu^n \mathbf{r}^n = \frac{\mathrm{d}}{\mathrm{d}t}\bigg|_I M_{\text{total}}\xi_O = M_{\text{total}}\dot{\xi}_O + \boldsymbol{\Omega}_O \times M_{\text{total}}\xi_O$$

where $\boldsymbol{\Omega}_O$ represents the angular velocity of the O frame relative to the inertial frame. Equation (2) can now be written as

$$\mathbf{P} = M_{\text{total}}\mathbf{V}_O + M_{\text{total}}\dot{\xi}_O + \boldsymbol{\Omega}_O \times M_{\text{total}}\xi_O \tag{3}$$

The expression for the total angular momentum about the origin of the O frame is given by

$$\mathbf{H}_O = \sum \mathbf{r}^n \times \mu^n \frac{\mathrm{d}}{\mathrm{d}t}\bigg|_I \mathbf{R}^n + \sum \mathcal{I}^n \boldsymbol{\Omega}^n = \sum \mathbf{r}^n \times \mu^n \mathbf{V}^n + \sum \mathcal{I}^n \boldsymbol{\Omega}^n \tag{4}$$

An alternate expression for the angular momentum is given by

$$\mathbf{H}_O = \sum \mathbf{r}^n \times \mu^n \frac{\mathrm{d}}{\mathrm{d}t}\bigg|_I (\mathbf{R}_O + \mathbf{r}^n) + \sum \mathcal{I}^n \boldsymbol{\Omega}^n = M_{\text{total}}\xi_O \times \mathbf{V}_O + \sum \mathbf{r}^n \times \mu^n \frac{\mathrm{d}}{\mathrm{d}t}\bigg|_O \mathbf{r}^n + \mathcal{I}_O \boldsymbol{\Omega}_O + \sum \mathcal{I}^n \boldsymbol{\Omega}^n \tag{5}$$

where the inertia matrix $\mathcal{I}_O$ is given by

$$\mathcal{I}_O = \sum \mu^n ((\mathbf{r}^n \cdot \mathbf{r}^n)\mathbb{I} - \mathbf{r}^n \mathbf{r}^n) \tag{6}$$

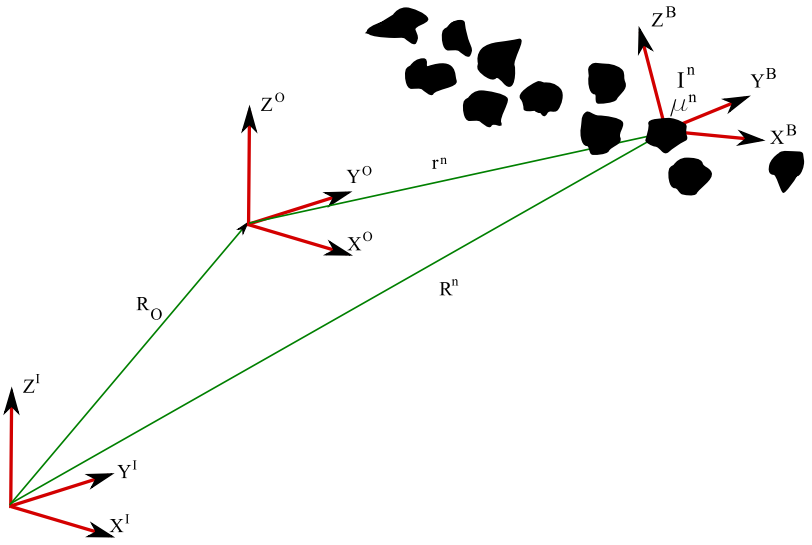

Fig. 2 Mean axis model schematic.

The rate of change of linear and angular momentum of the total system are given by:

$$\left.\frac{\mathrm{d}}{\mathrm{d}t}\right|_I \mathbf{P} = \left.\frac{\mathrm{d}}{\mathrm{d}t}\right|_O \mathbf{P} + \boldsymbol{\Omega}_O \times \mathbf{P} = M_{\text{total}}\dot{\mathbf{V}}_O + M_{\text{total}}\ddot{\xi}_O + \dot{\boldsymbol{\Omega}}_O \times M_{\text{total}}\xi_O + \boldsymbol{\Omega}_O \times M_{\text{total}}\dot{\xi}_O + \boldsymbol{\Omega}_O \times \mathbf{P} \tag{7}$$

$$\left.\frac{\mathrm{d}}{\mathrm{d}t}\right|_I \mathbf{H}_O = \left.\frac{\mathrm{d}}{\mathrm{d}t}\right|_O \mathbf{H}_O + \boldsymbol{\Omega}_O \times \mathbf{H}_O \quad = M_{\text{total}}\dot{\xi}_O \times \mathbf{V}_O + M_{\text{total}}\xi_O \times \dot{\mathbf{V}}_O + \sum \mathbf{r}^n \times \mu^n \left.\frac{\mathrm{d}^2}{\mathrm{d}t^2}\right|_O \mathbf{r}^n + \dot{\mathcal{I}}_O\boldsymbol{\Omega}_O + \mathcal{I}_O\dot{\boldsymbol{\Omega}}_O + \boldsymbol{\Omega}_O \times \mathbf{H}_O + \sum \mathcal{I}^n\dot{\boldsymbol{\Omega}}^n \tag{8}$$

where

$$\dot{\mathcal{I}}_O = \sum \mu^n(2(\mathbf{r}^n \cdot \dot{\mathbf{r}}^n)\mathbb{I} - \mathbf{r}^n\dot{\mathbf{r}}^n - \dot{\mathbf{r}}^n\mathbf{r}^n) \tag{9}$$

Application of Newton's laws give the following expressions for the rate of change of linear and angular momentum of the total system:

$$\left.\frac{\mathrm{d}}{\mathrm{d}t}\right|_I \mathbf{P} = \sum \mu^n \left.\frac{\mathrm{d}^2}{\mathrm{d}t^2}\right|_I \mathbf{R}^n = \sum \mathbf{f}^n \tag{10}$$

$$\left.\frac{\mathrm{d}}{\mathrm{d}t}\right|_I \mathbf{H}_O = \sum \left.\frac{\mathrm{d}}{\mathrm{d}t}\right|_I \mathbf{r}^n \times \mu^n \left.\frac{\mathrm{d}}{\mathrm{d}t}\right|_I \mathbf{R}^n + \sum \mathbf{r}^n \times \mu^n \left.\frac{\mathrm{d}^2}{\mathrm{d}t^2}\right|_I \mathbf{R}^n + \sum \left.\frac{\mathrm{d}}{\mathrm{d}t}\right|_I \mathcal{I}^n\boldsymbol{\Omega}^n = -\mathbf{V}_O \times \mathbf{P} + \sum \mathbf{r}^n \times \mathbf{f}^n + \sum \mathbf{m}^n \tag{11}$$

Now place the origin of the frame O at the center of gravity of the system. The subscript O on the right-hand side of velocity, moment of inertia, and angular momentum is now changed to cg to denote the shift of origin to the center of gravity. This sets the vector ξ_O and the corresponding rate term to zero. Equations (1) and (3) now give the expression for velocity of the center of gravity as

$$\mathbf{V}_{\text{cg}} = \frac{1}{M_{\text{total}}} \sum \mu^n \mathbf{V}^n \tag{12}$$

This prescribes the translational velocity of the origin of the O frame. Placing the origin of the O frame at the center of gravity of the system ensures that the linear momentum due to deformation is zero in the O frame.

Equations (4) and (5) when equated can be used to obtain multiple solutions to the angular velocity $\boldsymbol{\Omega}_O$. Choosing the angular velocity of the O frame to be

$$\boldsymbol{\Omega}_M = \mathcal{I}_{\text{cg}}^{-1} \sum \mathbf{r}^n \times \mu^n \mathbf{V}^n \tag{13}$$

implies

$$\sum \mathbf{r}^n \times \mu^n \left.\frac{\mathrm{d}}{\mathrm{d}t}\right|_O \mathbf{r}^n = 0$$

This choice of angular velocity of the O frame ensures that the deformation motion has zero angular momentum in the O frame. If the linear and angular velocity of the O frame are calculated as shown in Eqs. (12) and (13), respectively, the axis system O corresponds to the mean axis system M [12].

Equations (7) and (10) give the force equation as

$$M_{\text{total}}\dot{\mathbf{V}}_{\text{cg}} + \boldsymbol{\Omega}_M \times \mathbf{P} = \sum \mathbf{f}^n \tag{14}$$

and Eqs. (8) and (11) give the moment equation as

$$\mathcal{I}_{\text{cg}}\dot{\boldsymbol{\Omega}}_M + \dot{\mathcal{I}}_{\text{cg}}\boldsymbol{\Omega}_M + \sum \mathcal{I}^n\dot{\boldsymbol{\Omega}}^n + \boldsymbol{\Omega}_M \times \mathbf{H}_{\text{cg}} = \sum \mathbf{r}^n \times \mathbf{f}^n + \sum \mathbf{m}^n \tag{15}$$

where $\mathbf{P}$ and $\mathbf{H}_{\text{cg}}$ are calculated as shown in Eq. (1) and (4), respectively.

Equations (14) and (15) represent the equations of motion of the mean axis system with its origin at the center of mass of the system of bodies. If the relative position of the rigid bodies does not vary significantly, $\dot{\mathcal{I}}_{\text{cg}}$ can be approximated to be equal to zero. If the system of rigid bodies is taken to be a finite-state representation of a flexible body, Eqs. (14) and (15) represent the flight dynamics equations that are decoupled from the equations for structural dynamics under the small-deformation assumption. However, it is important to note that these equations are not completely decoupled due to the coupling through aerodynamic forces and moments.

Details regarding the calculation of mean axis parameters for the flexible flying wing using sensor readings of strains and curvatures are given in Section 4.2.2 and Section 4.6 of Ref. [13] and are not provided in this paper due to space constraints.

2. Kinematic Equations

For designing the control system, three axis systems are necessary. These are the root axis system R positioned at the center of the flying wing, an inertial axis system I with the same arrangement of axes, and the mean axis system M. The relative orientation of both the mean and the root axis system relative to the inertial axis system is defined using a 3-1-2 Euler angle rotation sequence. The rate of change of Euler angles is related to the inertial components of the angular velocity vector and the inertial position of the center of gravity is computed from the corresponding velocity components.

C. Control System Design

1. Guidance Algorithm

The nonlinear guidance algorithm used in this paper for path following was developed by Park et al. [11]. This guidance law was shown to give superior performance as compared with linear guidance laws in following curved paths. This is due to its ability to calculate the required lateral acceleration based on the commanded path ahead of the current vehicle position, and the use of the inertial velocity in calculating the acceleration to compensate for external disturbances such as wind [11].

Consider a trajectory defined by a sequence of points in the inertial frame as shown in Fig. 3. Denote the current inertial coordinates of the airplane by (x, y, h). Select a reference point on the trajectory at a specified distance L_1 ahead of the current position. Let V_g represent the velocity of the airplane in the X^IY^I plane, and η represent the angle between the velocity vector and the line to the reference point. The guidance algorithm gives the demanded lateral acceleration as [11]

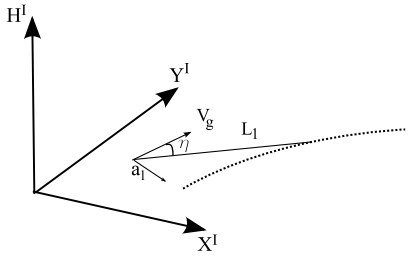

Fig. 3 Schematic for nonlinear guidance algorithm.

$$a_l^d = 2\frac{V_g^2}{L_1}\sin\eta \tag{16}$$

The lookforward distance L_1 also gives a lower bound on the radius of the circular ground path that can be followed as $L_1/2$ [11].

The altitude is controlled by specifying the commanded flight path angle based on the commanded and actual altitude and lookforward length L_h in the $Z^I - V_\infty$ plane. The commanded flight path angle γ_c is calculated as

$$\gamma_c = \frac{(h_c - h)}{L_h} \tag{17}$$

2. *Control Architecture for Flying Wings*

The dynamic inversion controller is designed using the force equation given by Eq. (14), the moment equation given by Eq. (15), and the kinematic equation given below:

$$\begin{Bmatrix} {}^M\Omega_{M1} \\ {}^M\Omega_{M2} \\ {}^M\Omega_{M3} \end{Bmatrix} = \begin{bmatrix} 0 & \cos\phi_{mi} & -\sin\phi_{mi}\cos\theta_{mi} \\ 1 & 0 & \sin\theta_{mi} \\ 0 & \sin\phi_{mi} & \cos\phi_{mi}\cos\theta_{mi} \end{bmatrix} \begin{Bmatrix} \dot{\phi}_{mi} \\ \dot{\theta}_{mi} \\ \dot{\psi}_{mi} \end{Bmatrix} \tag{18}$$

Applying the method of multiple time scales, the equations are inverted sequentially, and the output of inversion from one step is fed into the next [9,10]. This procedure is represented schematically in Fig. 4.

The inputs given to the controller are the commanded velocity V_c, commanded altitude h_c, commanded ground path in terms of the inertial $X - Y$ coordinates (x_c, y_c), and the lookforward lengths. Based on these inputs, the current position and ground speed, the guidance algorithm is used to compute the demanded lateral acceleration and commanded flight path angle. The magnitude of this demanded lateral acceleration is given by Eq. (16), and it is oriented in the direction normal to the projection of velocity vector in the inertial X^IY^I plane as shown in Fig. 3. This demanded lateral acceleration is specified in an intermediate frame V, which is offset from the inertial frame by a rotation χ about the Z^I axis. The components of the acceleration are given by

$${}^V\mathbf{a}^d = \begin{Bmatrix} a_l^d \\ 0 \\ 0 \end{Bmatrix}$$

where the left superscript indicates that the components are in the V frame.

In the second step, the force equations in Eq. (14) are inverted to find the magnitude of thrust required and the commanded pitch and roll angles while holding constant the commanded velocity along the inertial Z axis ($V_c \sin\gamma_c$) and inertial $X - Y$ plane ($V_c \cos\gamma_c$). The accelerations in the mean axis system are given by

$${}^M\dot{\mathbf{V}}_{\text{cg}} + {}^M\boldsymbol{\Omega}_M \times {}^M\mathbf{V}_{\text{cg}} = \mathcal{C}^{MV}{}^V\mathbf{a}^d \tag{19}$$

where the accelerations ${}^V\mathbf{a}^d$ are computed in the preceding step and the rotation matrix $\mathcal{C}^{MV}$ is given by

$$\mathcal{C}^{MV} = \mathcal{C}_2(\phi_{mi})\mathcal{C}_1(\theta_{mi})\mathcal{C}_3(\psi_{mi} + \chi) \tag{20}$$

Equation (14) is nonlinear in T, θ, and ϕ and is solved using a Newton-Raphson solver to obtain commanded values of thrust T, pitch angle θ_{mi_c}, and roll angle ϕ_{mi_c}. To solve this set of nonlinear equations, the velocity and angular velocity at any spanwise location has to be expressed as function of $V_c \cos\gamma_c$ and $V_c \sin\gamma_c$, and the angular velocity of the mean axis. This is done by assuming that the structure of the flying wing is rigid with its shape being the deformed shape at that time instant, and that aerodynamic forces and moments generated by structural vibrations are ignored. These new velocity and angular velocity values, which correspond to the motion of a deformed, rigid flying wing, are used in the controller to compute aerodynamic forces and moments.

In the next step, the demanded roll, pitch, and yaw rates are prescribed as

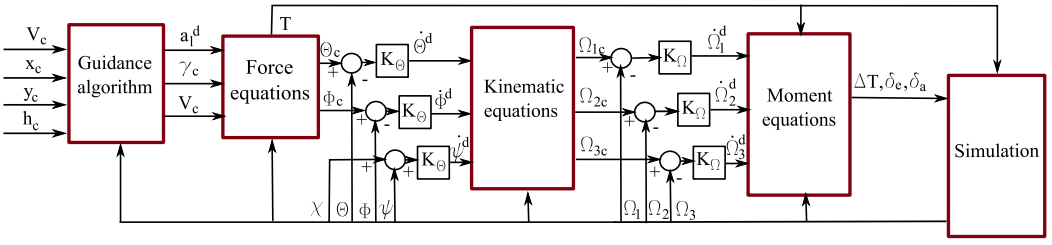

Fig. 4 Multistep nonlinear dynamic inversion applied to the mean axis model.

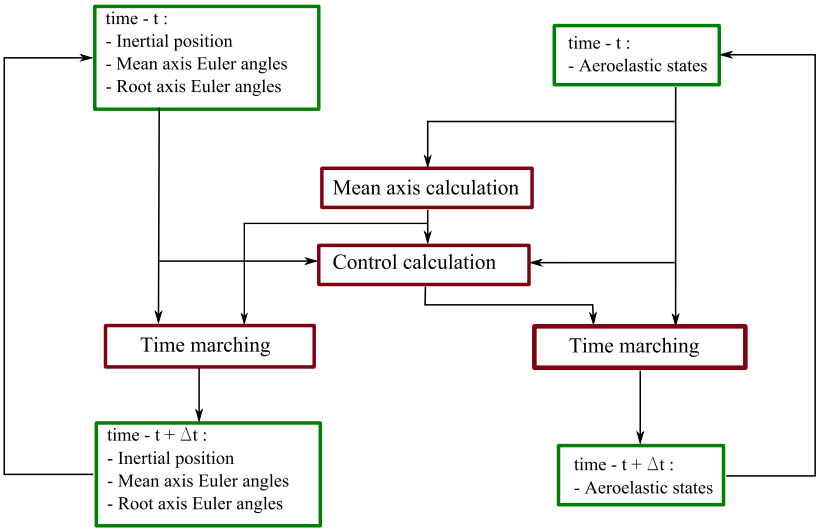

Fig. 5 Calculations carried out at each time step in the closed-loop.

Table 1 Geometric parameters for HALE configuration

$b = 73.06$ m	$C_{L_0} = 0$	$C_{L_\alpha} = 2\pi$	$C_{L_\delta} = 1$	$C_{D_0} = 0.01$
$c = 2.44$ m	$C_{m_0} = 0.025$	$C_{m_\alpha} = 0$	$C_{m_\delta} = -0.25$	$\mu = 8.93$ kg/m
	$I_{xx} = 4.15$ kg m	$I_{yy} = 0.69$ kg m	$I_{zz} = 3.46$ kg m	

Table 2 Elastic parameters for HALE configuration

Number of nodes	25
Number of unsteady aerodynamic states at each element	6
Payload mass variation at center	0 kg to 250 kg
Wing tip dihedral	5°
Position of wing tip dihedral	12.19 m from wing tip
Sectional center of gravity	25% chord
Elastic axis position	25% chord
Torsional rigidity	0.825×10^6 N m^2
Bending rigidity	1.03×10^6 N m^2
Bending rigidity, chordwise	12.39×10^6 N m^2

$$\dot{\phi}^{\,d}_{mi} = K_\theta(\phi_{mi_c} - \phi_{mi}) \tag{21}$$

$$\dot{\theta}^{\,d}_{mi} = K_\theta(\theta_{mi_c} - \theta_{mi}) \tag{22}$$

$$\dot{\psi}^{\,d}_{mi} = -K_\theta(\chi + \psi_{mi}) \tag{23}$$

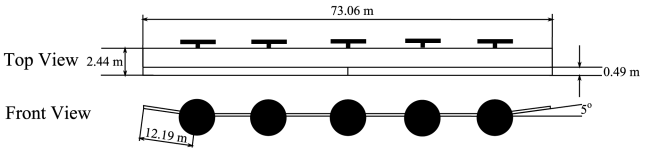

Fig. 6 Schematic of configuration.

The dynamics are prescribed such that the controller tries to drive the states to the prescribed values with a time constant that is inversely proportional to the gain K_θ. These three rates are used to compute the commanded angular velocities ${}^M\boldsymbol{\Omega}_{Mc}$ using Eq. (18). In the final step, the demanded angular velocity rates are computed as

$${}^M\dot{\boldsymbol{\Omega}}^{\,d}_M = K_\Omega({}^M\boldsymbol{\Omega}_{Mc} - {}^M\boldsymbol{\Omega}_M) \tag{24}$$

Equation (15) is now inverted to find the differential thrust required for yaw control and the required aileron and flap deflections.

D. Overview of Closed-Loop Simulation

The schematic of the closed-loop system is shown in Fig. 5. Given a state vector of the complete aeroelastic system at time t, a module computes the velocity, angular velocity, linear and angular momentum, and moment of inertia at that time instant in the mean axis. These values, together with the inertial position and Euler angles, are used to compute the control input to be applied to the system from time t to $t + \Delta t$. The time-marching algorithm is implemented at each time step on two sets of equations. The first set corresponds to the complete aeroelastic model which has $(21 \times N) + [(N - 1) \times m]$ states, where N corresponds to the number of nodes and m corresponds to the number of unsteady aerodynamic states at each element. The second set consists of kinematic equations relating Euler angle rates to the angular velocity applied to both the root and the mean axis and the equations for calculation of the position of the center of gravity of the flying wing in the inertial frame. Details of the time-marching

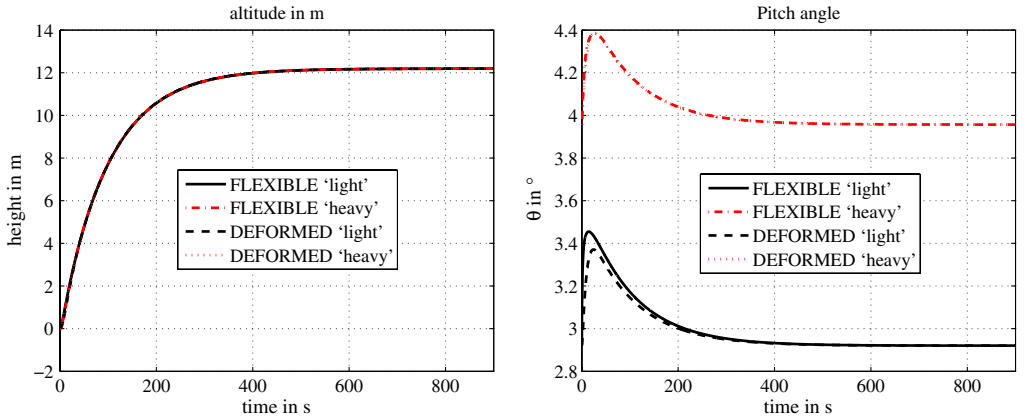

a) Altitude history **b) Pitch angle history**

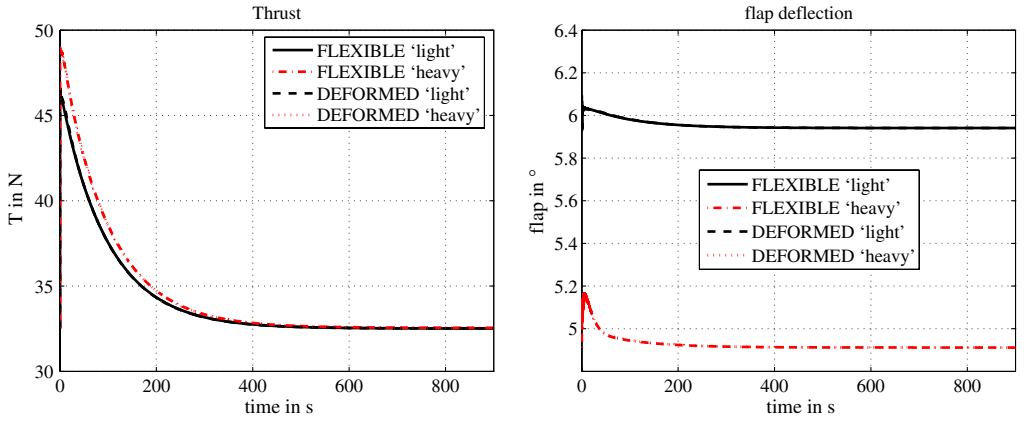

c) Thrust history **d) Flap history**

Fig. 7 Straight and level path with initial vertical offset.

integration scheme that was used are available in Section 4.4 of Ref. [13] and are not provided in this paper due to space constraints.

IV. Results

A. Open-Loop Verification

The aeroelastic code used for carrying out time-marching simulations was verified for the cantilevered Goland wing. Analytical and computational results were compared for flutter, divergence and control reversal speed, free vibration frequencies, and Euler bucking load. Results from the verification process are given in Ref. [13].

B. Sample Configuration

1. Specifications of the Configuration

This configuration used in this paper is identical to the one studied in Ref. [7] except for the following two features. The three landing gear pods have been eliminated, and the torsional stiffness has been increased by a factor of 5 to prevent control reversal. Parametric values used to define the configuration are given in Tables 1 and 2. A schematic of the configuration is given in Fig. 6.

Two payload configurations are studied: a light configuration with a 45.35 kg nodal mass at the center of the wing, and a heavy configuration with a 181.4 kg nodal mass at the center of the wing. In addition to the difference in payload, the following two configurations are compared: a rigid flying wing defined using static aeroelastic deformation at trim for a given flight condition (deformed), and a flexible flying wing configuration (flexible). Only representative results are presented in this paper. Closed-loop results for other path-following cases are given in Ref. [13].

2. Gain Selection

For the multistep dynamic inversion method used in this paper to work, it is important to ensure that the time scale for the prescribed faster dynamics is lower than the time scale for the prescribed slower dynamics. The equations for the rate of change of angular velocity constitute the faster dynamics and are the first ones to be addressed. The selection of these gains is explained using the equation for the rate of change of angular velocity along the X^M axis. Because the dynamic inversion controller inverts the moment equation exactly the new dynamics for the rate of change of angular momentum is given by Eq. (24) as

$$ {}^M\dot{\Omega}_{M_1} = {}^M\dot{\Omega}^d_{M_1} = K_\Omega({}^M\Omega_{M_{1c}} - {}^M\Omega_{M_1}) \tag{25} $$

Assuming the roll angle ϕ_{mi} to be zero, Eq. (25) can be rewritten using Eqs. (18) and (22) as

$$ \ddot{\theta}_{mi} = K_\Omega(K_\theta(\theta_{mi_c} - \theta_{mi}) - \dot{\theta}_{mi}) $$

which gives the following second-order equation for θ_{mi}:

$$ \ddot{\theta}_{mi} + K_\Omega\dot{\theta}_{mi} + K_\Omega K_\theta\theta_{mi} = K_\Omega K_\theta\theta_{mi_c} $$

The values of K_Ω and K_θ are chosen to be 1 rad/s and 0.1 rad/s, respectively, which gives the following values for frequency and damping:

$$ \omega_n = \sqrt{K_\Omega K_\theta} = 0.316 \text{ rad/s} \qquad \zeta = \frac{1}{2}\sqrt{\frac{K_\Omega}{K_\theta}} = 1.581 $$

For an overdamped second-order system, the time constant for the exponential decay of the amplitude is given by $1/\zeta\omega_n$. This time

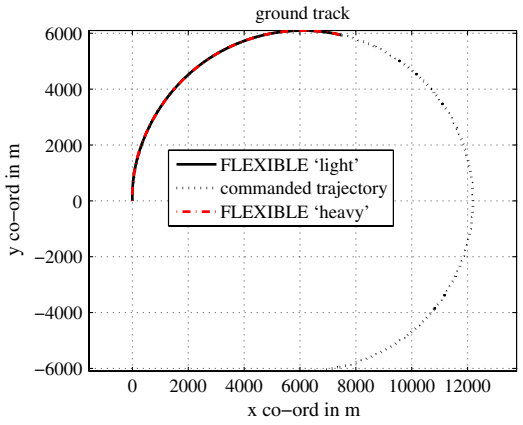

a) Ground track history

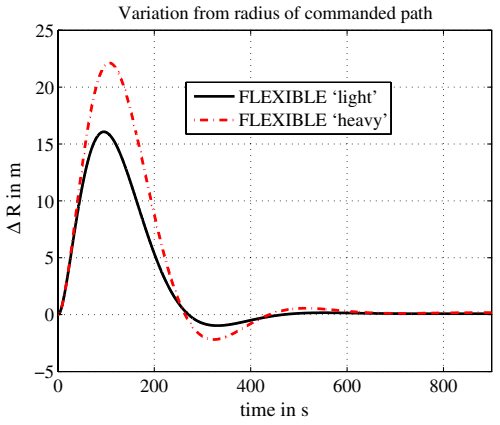

b) Δ R history

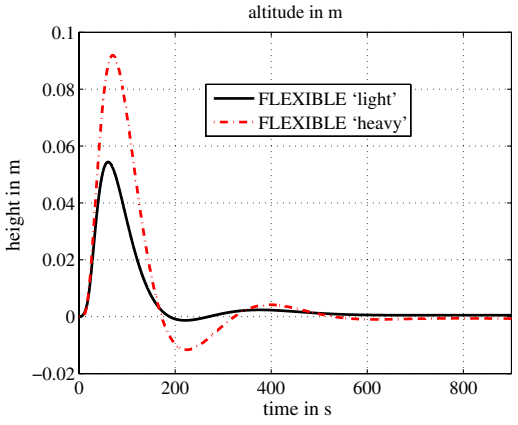

c) Altitude history

Fig. 8 Curved ground path with no initial offset.

constant can be used as the characteristic time scale for the system response. For these gain values of K_Ω and K_θ, this time scale has a value of 2 s.

The time scales for the slow dynamics is determined by the guidance equations for path following and altitude change. The rate of change of altitude can be written using Eq. (17) as

$$\dot{h} = V_c \sin\gamma_c = \frac{V_c}{L_h}(h_c - h)$$

The above first-order system has a time constant given by L_h/V_c. For a prescribed flight speed of 12.19 m/s, the reference length L_h is chosen to be 1219 m, giving a time-constant of 100 s. The guidance law linearized for following a straight-line path becomes a second-order equation in the lateral-offset distance and has a frequency and damping value given by [11]

$$\omega_n = \frac{\sqrt{2}V_c}{L_1} \qquad \zeta = \frac{1}{\sqrt{2}} = 0.707$$

For a lookforward length L_1 of 1219 m, the characteristic time scale $1/\zeta\omega_n$ has a value of 100 s. These gain values ensure sufficient separation between the time scales for the fast and slow dynamics and are used in all simulations presented in this section.

C. Closed-Loop Results

1. *Straight and Level Path with Initial Vertical Offset*

The first set of simulations are for straight climbing flight. The simulation is initialized with the airplane trimmed in straight and level flight at 12.19 m/s along the inertial Y-axis at the origin of the inertial reference frame and is commanded to increase its altitude by 12.19 m while maintaining its heading. Two payload cases are considered: the light payload case corresponding to a nodal mass at the center of 45.35 kg, and a heavy payload case corresponding to a nodal mass of 181.4 kg. For each of the two payload cases, simulations are presented for the fully flexible flying wing model (denoted by "flexible" in the graphs) and a rigid-body model based on the deformed shape at straight and level trim (denoted by "deformed" in the graphs). Because the lateral variables are unperturbed in this simulation, only the longitudinal variables have been plotted in Figs. 7. These are the altitude of the airplane, the pitch angle of the mean axis, the commanded thrust, and the commanded flap deflection.

The altitude of the airplane shows a first-order response and converges to the commanded altitude. The pitch angle of the mean axis shows an initial perturbation during climb before converging back the value for straight and level flight. The commanded thrust value shows an abrupt jump at the very first time instant corresponding to the step change in commanded altitude from the initial condition. The commanded flap deflection for the flexible configuration exhibits high-frequency oscillations during the transient response for both the light and the heavy payload cases due to an abrupt change in commanded value. These oscillations are due to the coupling of the controller with a low-frequency aeroelastic bending mode and die out as time progresses. Even in the presence of these oscillations, the mean value of the commanded flap deflection shows the same trend as the commanded flap deflection for the corresponding deformed configuration.

2. *Curved Ground Path with No Initial Offset*

The next set of simulations is for following a curved ground path. The commanded path is defined to be a circle of fixed radius in the inertial XY plane. To study the ground path of the airplane relative to its commanded path, a new parameter is plotted for the next two sets of simulations. This new parameter ΔR is given by

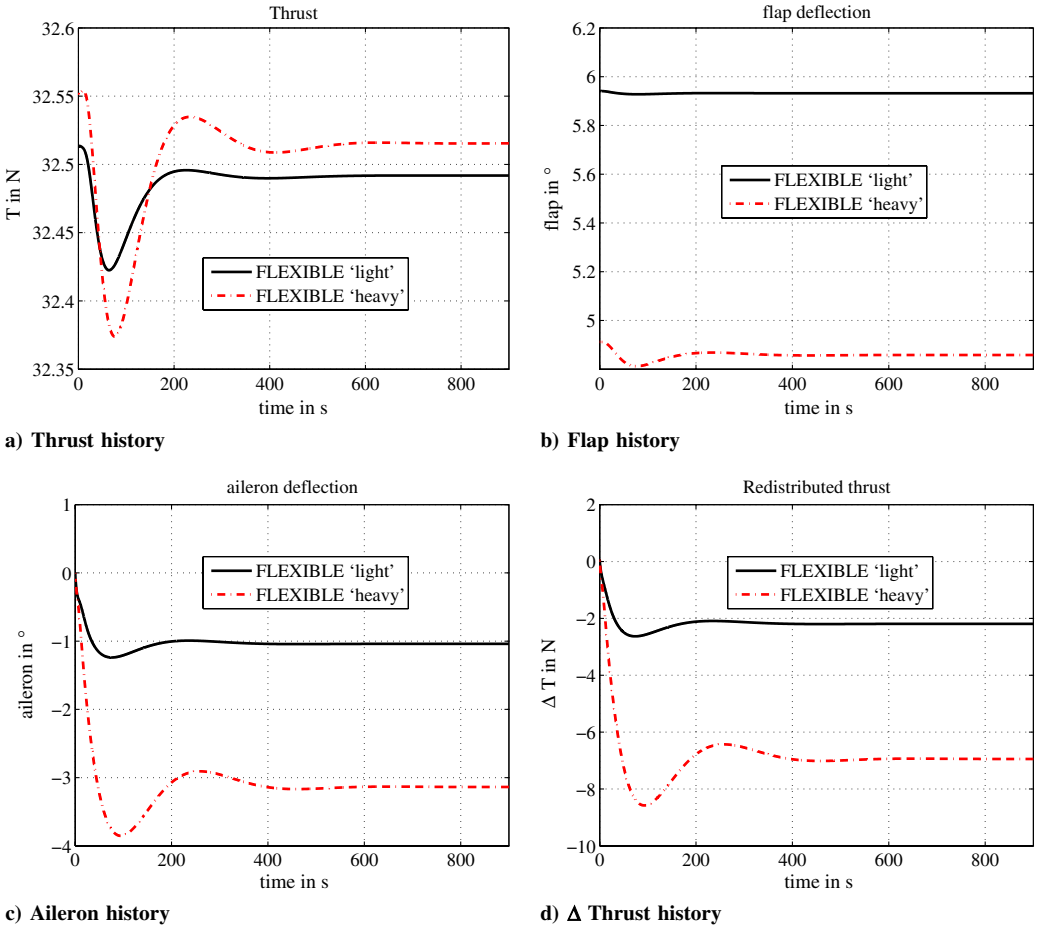

a) Thrust history **b) Flap history**

c) Aileron history **d) Δ Thrust history**

Fig. 9 Curved ground path with no initial offset.

$$\Delta R(t) = R(t) - R_c$$

where $R(t)$ is given by

$$R(t) = \sqrt{(x(t) - x_0)^2 + (y(t) - y_0)^2}$$

In the preceding equations (x_0, y_0) represents the origin of the commanded flight path, $([x(t), y(t)]$ represent the inertial coordinates of the airplane, and R_c represents the radius of the commanded flight path.

The simulation is initialized with the airplane trimmed in straight and level flight at 12.19 m/s along the inertial Y-axis at the origin of the inertial coordinate system. The airplane is commanded to track a circular ground path of radius 6096 m with an origin at (6096, 0) m while maintaining its current altitude. Unlike the preceding case, the initial state of the flying wing and the final steady state correspond to two different trim conditions for this trajectory. Because of the nature of this trajectory, the lateral dynamics of the airplane are significant compared with the longitudinal dynamics. Both the light and the heavy payload cases for the flexible configuration are studied. A total of seven parameters are plotted in Figs. 8 and 9. These are the ground path, ΔR, altitude, and the four control parameters. The corresponding Euler angle time histories are available in Ref. [13].

For both the light and the heavy payload case, the parameter ΔR and the altitude converge exactly to the commanded value. For both cases, the roll angle converges to a nonzero value corresponding to banked flight, while the yaw angle increases linearly after the transients die down. Though the airplane is commanded to maintain its altitude, the longitudinal control variables (thrust and flap deflection) do not converge to their initial value as the trim condition for turning flight is different from the trim for turning flight. The aileron deflection and differential thrust ΔT converge to a nonzero value corresponding to steady turning flight.

The next set of simulations studies the variation of closed-loop response for turning flight with decreasing turn radius. The initial position of the flying wing is chosen to be at the origin of the inertial reference frame, and it is commanded to track a circle of a given radius while maintaining its altitude. For a given turn radius R, the origin of the circle to be tracked is chosen to be at $(R, 0, 0)$ m in the inertial frame. Simulations are carried out for turn radii of 6096 m, 4572 m and 3048 m.

Simulations show that the flying wing is able to successfully track circles of radii 6096 m and 4572 m but is unable to track a circle of 3048 m. This limitation of the controller is explained by Fig. 10b. The plot shows the variation of ΔT with time, along with a plot of $-T/2$ for the 3048 m turn radius case. As $|\Delta T|$ reaches $T/2$, the thrust at one of the outboard engines goes to zero and yaw control saturates. However, the simulation is continued until the thrust calculated by the controller for the engine at the center T reaches zero, when the simulation is terminated. It is observed that once yaw control saturates, the airplane is no longer able to follow the commanded path and ultimately diverges. This saturation does not occur for the other two cases, and the flying wing is able to successfully follow the corresponding ground paths. For the cases corresponding to the two larger radii, ΔR and altitude go to zero as the transients die down, and aileron deflection, ΔT, and roll angle converge to a nonzero value corresponding to the equilibrium for turning flight.

To overcome the inability of the flying wing to turn with a radius of 3048 m, the initial position of the flying wing is moved to $(0, -L_1, 0)$ m, where L_1 is the lookforward distance of the guidance

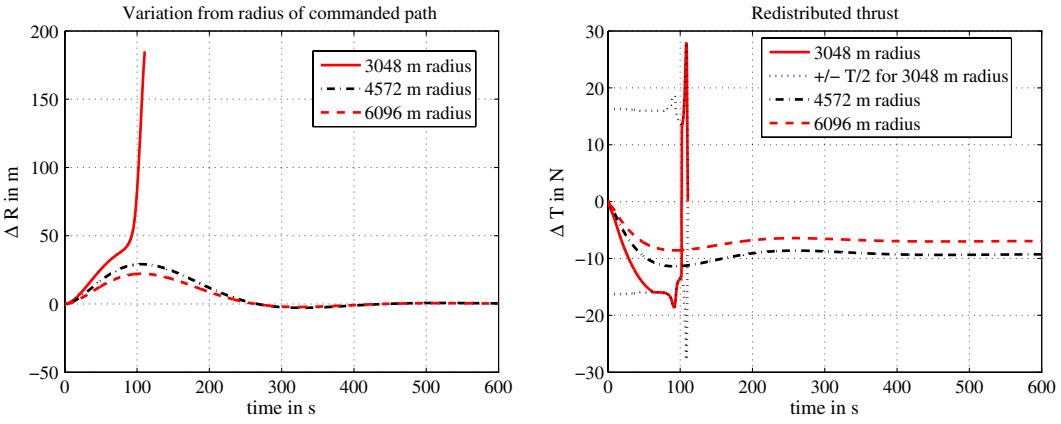

a) Δ R history **b) Δ Thrust history**

Fig. 10 Curved ground path with no initial offset (small radii).

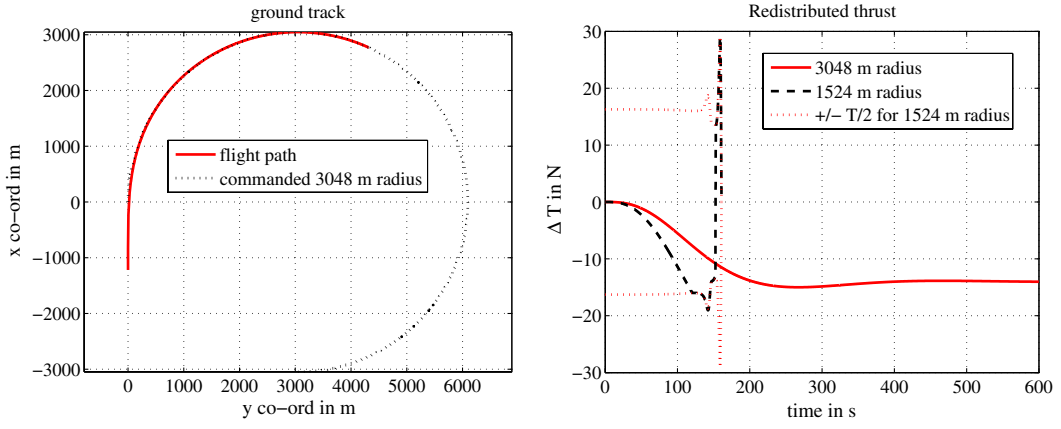

a) Ground track history **b) Δ Thrust history**

Fig. 11 Curved ground path with no initial offset (guidance law activated early).

law. This change in initial position tells the controller of the circular path to be followed before the flying wing actually reaches the origin of the inertial XY plane, which is a point on the circular path. With this change, the flying wing is able to successfully follow a circle of radius 3048 m, as seen from Fig. 11. However, when the radius is decreased to 1524 m, the flying wing is no longer able to follow the corresponding circular ground path as the yaw control saturates, as seen in Fig. 11b.

3. *Path-Following with Abrupt Change in Payload Mass*

This set of simulations involves an abrupt change in the payload mass carried by the flexible flying wing. The airplane is trimmed in straight and level flight at 12.19 m/s at the origin of the inertial reference frame with the velocity vector along the inertial Y-axis and is commanded to maintain its heading and altitude. The initial payload at the center of the flying wing is set as 181.4 kg (corresponding to the heavy case). At $t = 50$ s, the payload is decreased abruptly. The two cases considered correspond to a decrease in payload by 50 and 25%, respectively, and are plotted in Fig. 12.

The change in payload mass also results in an abrupt change in the equilibrium aeroelastic state vector. Simulations show that the controller is able to control the transients due to the abrupt change in payload mass and drive the states to the new equilibrium condition. The change in payload mass causes the altitude to increase initially due a drop in the mass of the airplane as shown in Fig. 12b. The altitude of the airplane then decreases before coming back to its initial value. Once again, the transient flap response exhibits high-frequency oscillations due to coupling with bending modes. The

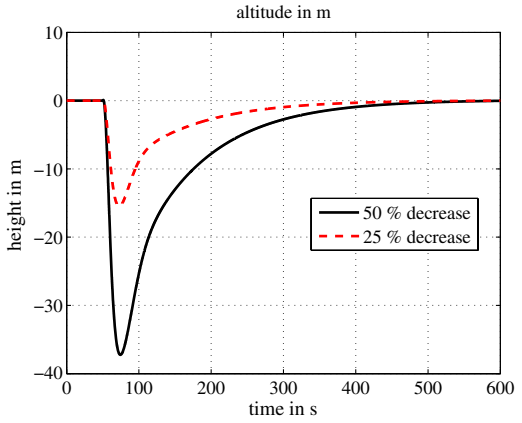

a) Altitude history

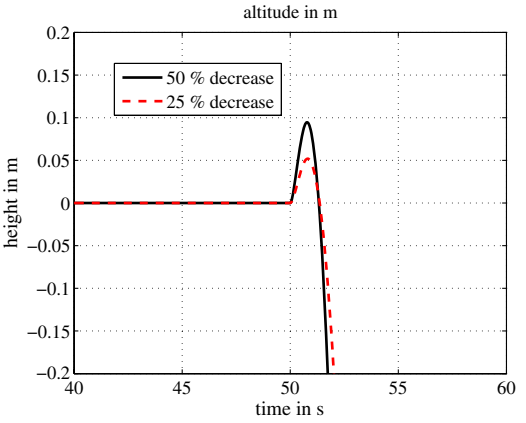

b) Altitude history showing detail at t = 50s

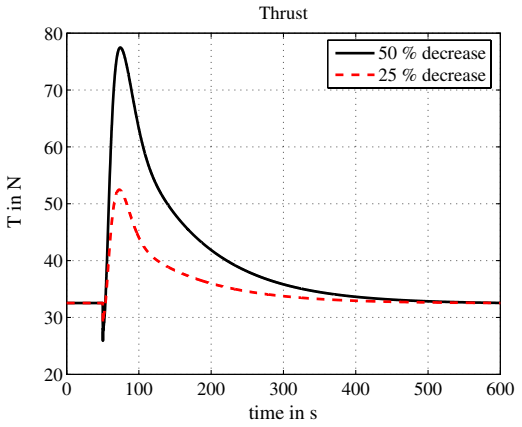

c) Thrust history

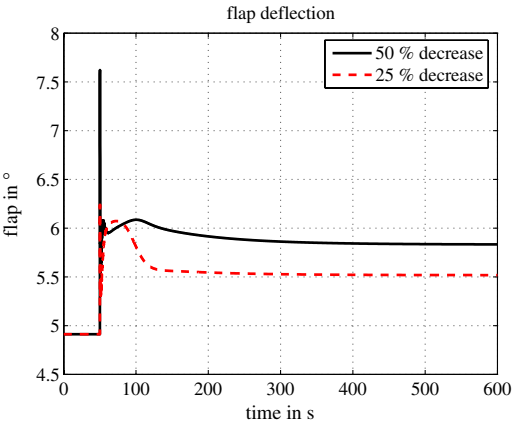

d) Flap history

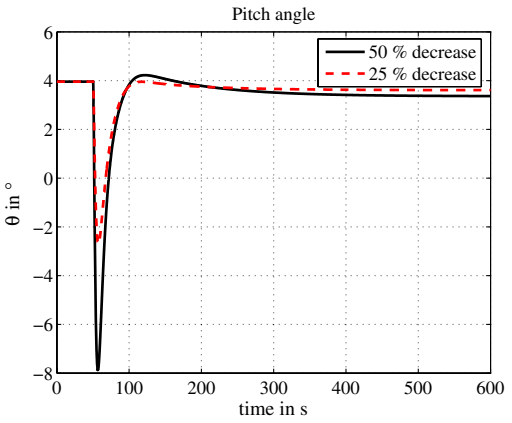

e) Pitch angle history

Fig. 12 Path following with abrupt change in payload mass.

magnitude of the transient response is shown to increase with an increase in the change in the payload mass.

V. Conclusions

The objective of this paper was to design a flight control law for path following for a flexible, high aspect-ratio flying wing. Using the concept of the mean axis, a 6-degree-of-freedom reduced-order model of the flight dynamics is constructed that minimizes the coupling between rigid-body modes and the structural dynamics while accounting for the static aeroelastic deformation of the flying wing. This mean axis model does not assume small deformation, unlike the model used by Milne. Multistep nonlinear dynamic inversion applied to this reduced-order model is coupled with a nonlinear guidance law to design a flight controller for path following. The configuration of the flying wing used in the reduced-order model is updated at each time instant to account for static aeroelastic deformation. The controls computed by this flight controller are used as inputs to a time-marching simulation of the integrated model of aeroelasticity and flight dynamics. Simulation results presented in this paper show that the controller is able to successfully follow both straight line and curved ground paths while maintaining or moving to the desired altitude. The controller is also shown to be able to handle an abrupt change in the external loading, which is simulated in this paper by a step change in the payload mass.

References

[1] Noll, T. E., Brown, J. M., Perez-Davis, M. E., Ishmael, S. D., Tiany, G. E., and Gaier, M., "Investigation of the Helios Prototype Aircraft Mishap," NASA, 2004.

[2] Gregory, I. M., "Dynamic Inversion to Control Large Flexible Aircraft," *Proceedings of the AIAA Guidance, Navigation, and Control Conference and Exhibit*, AIAA Paper 1998-4323, 1998.

[3] Gregory, I. M., "Modified Dynamic Inversion to Control Large Flexible Aircraft - What's Going On?," *Proceedings of the AIAA Guidance, Navigation, and Control Conference and Exhibit*, AIAA Paper 1999-3998, 1999.

[4] Gregory, I. M., "Stability Result for Dynamic Inversion Devised to Control Large Flexible Aircraft," *Proceedings of the AIAA Guidance, Navigation, and Control Conference and Exhibit*, AIAA Paper 2001-4284, Aug. 2001.

[5] Shearer, C. M., and Cesnik, C. E. S., "Nonlinear Flight Dynamics of Very Flexible Aircraft," *Journal of Aircraft*, Vol. 44, No. 5, Sep.–Oct. 2007, pp. 1528–1545. doi:10.2514/1.27606

[6] Shearer, C. M., and Cesnik, C. E. S., "Trajectory Control for Very Flexible Aircraft," *Journal of Guidance, Control, and Dynamics*, Vol. 31, No. 2, Mar.–Apr. 2008, pp. 340–357. doi:10.2514/1.29335.

[7] Patil, M. J., and Hodges, D. H., "Flight Dynamics of Highly Flexible Flying Wings," *Journal of Aircraft*, Vol. 43, No. 6, Nov.–Dec. 2006, pp. 1790–1798. doi:10.2514/1.17640

[8] Raghavan, B., and Patil, M. J., "Flight Dynamics of High Aspect-Ratio Flying Wings: Effect of Large Trim Deformation," *Journal of Aircraft*, Vol. 46, No. 46, Sept. 2009, pp. 1808-1812.

[9] Snell, S. A., Enns, D. F., and Garrard W. L. Jr., "Nonlinear Inversion Flight Control for a Supermaneuverable Aircraft," *Journal of Guidance, Control, and Dynamics*, Vol. 15, No. 4, July–Aug. 1992, pp. 976–984. doi:10.2514/3.20932.

[10] Bugajski, D. J., and Enns, D. F., "Nonlinear Control Law with Application to High Angle-of-Attack Flight," *Journal of Guidance, Control, and Dynamics*, Vol. 15, No. 3, May–Jun. 1992, pp. 761–767. doi:10.2514/3.20902.

[11] Park, S., Deyst, J., and How, J. P., "Performance and Lyapunov Stability of a Nonlinear Path-Following Guidance Method," *Journal of Guidance, Control, and Dynamics*, Vol. 30, No. 6, Nov.–Dec. 2007, pp. 1718–1728. doi:10.2514/1.28957.

[12] Milne, R. D., "Dynamics of the Deformable Aeroplane," R&M, British Aeronautical Research Council, 3345, London, 1964.

[13] Raghavan, B., "Flight Dynamics and Control of Highly Flexible Flying-Wings," Ph.D. thesis, Virginia Polytechnic Institute and State Univ., Blacksburg, VA, March 2009.